

Design, Preparation, and Mechanical Property Investigation of Ti-Ta 3D-Auxetic Structure by Laser Powder Bed Fusion

Mu Gao, Dingyong He, Xu Wu, Zhen Tan, and Xingye Guo*

In recent years, Ti-Ta alloy has become a hot material in orthopedic implants. At the same time, the metal lattice structure with a negative Poisson's ratio has a great prospect in the application of implants due to its unique mechanical properties. Herein, an antichiral three-dimensional polyhedron (A3P) lattice structure with negative Poisson's ratio is designed. This lattice structure is prepared by laser powder bed fusion (LPBF) technology using Ti-Ta alloy as the feedstock material. The surface morphology and relative density of the Ti-Ta samples built with different laser scanning speeds are compared for the optimization of the Ti-Ta's LPBF parameter. Then, the A3P structure of the Ti-Ta alloy is fabricated using the optimized LPBF parameters. The negative Poisson's ratio effect of the A3P structure is verified by finite element analysis (FEA) and compared with experimental results. The compression test results show that the yield strength and elastic modulus of the A3P structure are 9.2 MPa and 0.14 GPa, respectively, which is suitable for the orthopedics application. A3P structure has higher fracture energy compared with diamond structure, indicating it can absorb more energy in the fracture process. A3P shows a promising prospect in the application of orthopedics implantation.

1. Introduction

Metamaterial is a novel artificial material that has supernormal physical properties, such as optical, acoustic, thermal, electromagnetic, and mechanical properties.^[1,2] These special properties are designed by the internal artificial structure which does not exist in natural materials.^[3,4] In recent years, many scholars have conducted research on mechanical metamaterials.^[5–7] The lattice structure is one of the typical mechanical metamaterials. It is characterized by a strut or solid part arranged in a particular and periodic sequence which is similar to the arrangement of atoms in a crystal.^[4] Compared with

traditional materials, the lattice structures have high strength-to-weight ratio, lower modulus, higher strike resistance, more suitable biocompatibility, and better mechanical response.^[8–10] It has great prospects in aviation, biomedicine, energy absorption, and architectural construction.^[8,11] The component elements of a lattice structure, such as struts or solid parts, can be purposely designed to build the lattice structure with auxetic behavior, which is also named as the negative Poisson's ratio effect.^[12] In the tensile process, the auxetic material expands perpendicular to the stretching direction, and the elastic modulus decreases with the increase of the volume compression ratio. However, in the compressive process, it shrinks perpendicular to the compressive direction, and the elastic modulus increases with the increase of the compression ratio. This mechanical behavior is just opposite to the traditional material from natural world with positive Poisson's ratio. Therefore, the auxetic structure has

higher shear resistance and higher energy absorption efficiency, which has great potential in the application of orthopedic implants.^[13] H. M. Kolken^[14] designed hip stems with negative Poisson's ratios. This orthopedic implant both stimulates bone regeneration and prevents wear particles from entering the interface of the bone and the implant. The wear particles cause an inflammatory response, which promotes the formation of loose interface tissue and ultimately implant loosening.^[15–17]

The typical negative Poisson's ratio structures are always designed with two basic components: rigid rotators^[18] and concaved polygonal modules.^[19] The former includes various chiral and antichiral structures,^[20,21] and the latter includes concaved-hexagonal structures,^[22] double arrow structures,^[23] star structures.^[24,25] Most 3D auxetic structures were designed based on typical 2D auxetic structures expanding at least in two of the X, Y, or Z directions. In this case, the 3D auxetic structures were different in all directions, leading to anisotropic mechanical behaviors.^[5] To overcome this problem, H. Huang,^[26] Q. Q. Zhang,^[27] and X. Fei^[28] proposed a special 3D-anti-tetra-chiral structure prepared by LPBF technology and the meta-architecture with negative Poisson's ratio effect was studied in their literatures. However, this structure contained many cantilever struts which were disadvantageous for building by LPBF.^[5] It is difficult to construct 3D auxetic structures with

M. Gao, D. He, X. Wu, Z. Tan, X. Guo
Faculty of Materials and Manufacturing
Beijing University of Technology
Beijing 100124, P. R. China
E-mail: xyguo@bjut.edu.cn

D. He
Beijing Engineering Research Center of Eco-materials and LCA
Beijing 100124, P. R. China

 The ORCID identification number(s) for the author(s) of this article can be found under <https://doi.org/10.1002/adem.202300242>.

DOI: 10.1002/adem.202300242

traditional fabrication technology due to the complex internal characteristics. However, additive manufacturing (AM) has significant advantages for the preparation of complex lattice structures.^[29] In AM process, the digital model of a workpiece is sliced into many 2D patterns of specified layers. Then, the AM machine builds these layers in order and finally prepares the workpiece completely, which can realize the construction of internal holes and features of the workpiece.^[30] In addition, the AM process can refine the grain inside the workpiece and improve its mechanical properties.^[31]

As a new type of biomaterial, Ti-Ta alloy has a great prospect in the application of orthopedic implants.^[32] The advantages of Ti-Ta alloy applied as an orthopedic implant are high strength, low modulus, and good corrosion resistance, which can alleviate the stress shielding of implants.^[33] In addition, Ti-Ta alloy will not release toxic metal ions and cause lesions in the service process, which ensures the safety of the human body. Some scholars reported the application of Ti-Ta alloy in biology. In S. Huang's study,^[32] porous Ti-Ta scaffolds fabricated using LPBF were biocompatible with comparable biological properties as Ti-6Al-4V and commercially pure titanium, based on the results obtained from cell culture with human osteosarcoma cell line SAOS-2. Meanwhile, the Ti-Ta alloy prepared by AM process had excellent mechanical properties and was also reported. Y. Zhou^[34] found that when the Ta content was at 25 wt%, Ti-Ta alloy had the lowest elastic modulus, suitable density, and the highest ratio of strength to modulus and exhibits the best mechanical compatibility. Ti-25Ta was considered a promising candidate for metallic biomaterials in the future. E. G. Brodie^[35] successfully manufactured Ti-25Ta samples by LPBF. This work demonstrates that the LPBF Ti-25Ta displayed promising mechanical properties for biomedical implant applications. The yield stress normalized fatigue performance of the Ti-25Ta material was superior to pure Ti and Ti-6Al-4V, due to the solution strengthening of the titanium and retained ductility.

In the present study, a new antichiral three-dimensional polyhedron (A3P) auxetic structure was designed and fabricated with the material of Ti-Ta alloy by LPBF technology. The content of Ti:Ta was 75 wt%:25 wt%. First, the mixed Ti-Ta powder was used to prepare specific samples by LPBF technology with different process parameters. The processing parameters were optimized based on the surface roughness and relative density of the bulk samples. Then, the mechanical properties of LPBF-built bulk Ti-Ta alloy were also evaluated as a prerequisite material data for the following simulations and design analysis. Based on the above results, the designed auxetic A3P structure in this study was prepared using the LPBF technology with the optimized process parameters. The mechanical properties of A3P samples were analyzed by experimental and finite element analysis (FEA) simulations. Uniaxial compression tests were conducted to study the elastic and failure behaviors of the Ti-Ta A3P lattice structure. The traditional diamond lattice structure was also prepared as the comparison sample for the investigation of the A3P structure.

2. Experimental Section

2.1. Design of the A3P Structure

The idea of the A3P auxetic structure was initially proposed based on a 2D antichiral quadrilateral, which was a traditional 2D

negative Poisson's ratio structure. The projection shapes of the A3P structure in the X, Y, and Z directions were 2D antichiral quadrilateral, which ensured the orthotropic behavior in mechanical properties for the A3P structure. As a special lattice structure, the fundamental element of the A3P metamaterial structure was also cylindrical struts and connection nodes. The A3P metamaterial structure designed in this work was a novel three-level hierarchical lattice structure, including the A3P unit-cell (A3P-UC) as the first-level structure, the A3P intermediate-module (A3P-IM) as the second level, and the whole A3P sample (A3P-S) as the third-level structure, as shown in Figure 1, 2 and 3, respectively. The A3P-UC and A3P-IM were imperative and fundamental component for the building of any kind of A3P structures. The third-level structure A3P-S was a combination of an arbitrary amount of A3P-IM, which could be worked as an independent part or sample with the negative Poisson's ratio.

The schematic images of A3P-UC are shown in Figure 1. The tilt angle θ of the A3P-UC to the horizontal plane (XY plane) was 30°, as shown in Figure 1. A coordinate system was established with the geometric center of the A3P-UC as the origin (O). The A3P-UC totally contained 14 nodes, including 6 primary nodes (PN) and 8 accessory nodes (AN). The PN was the connection node between the A3P-UCs when the second- and third-level A3P structure was formed, and the AN did not contact another A3P-UC. The coordinates of each node in an A3P-UC are listed in the following Table 1.

A single A3P-IM containing 8 A3P-UC was built by mirroring the A3P-UC along the X, Y, and Z directions, respectively, as shown in Figure 2. Finally, a complete A3P-S was obtained by

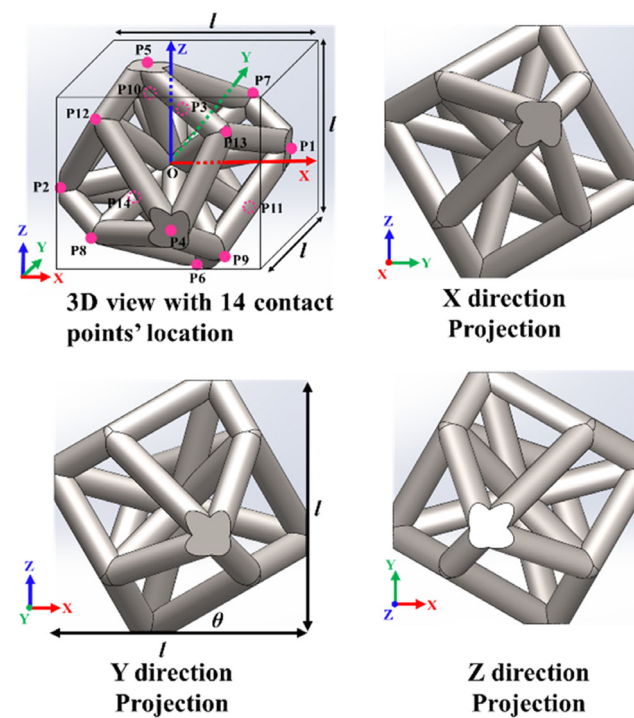


Figure 1. Schematic of the A3P-UC and the position of the contact points.

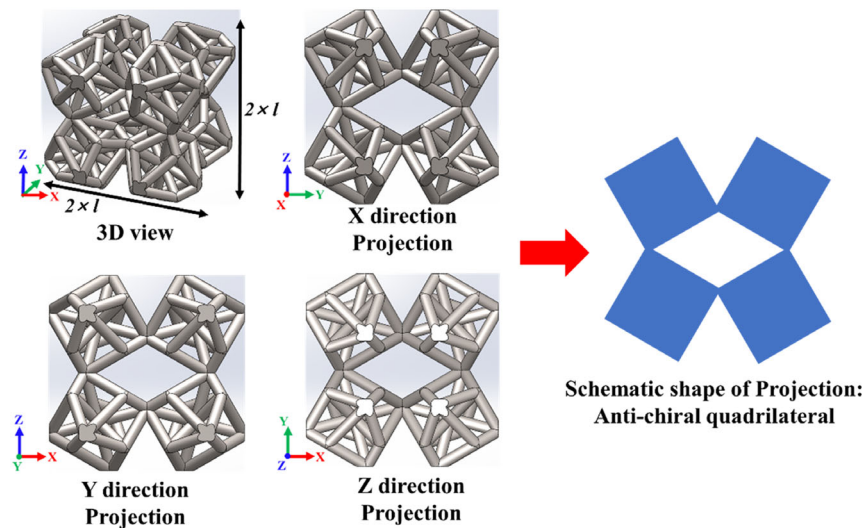


Figure 2. Schematic of the A3P-IM.

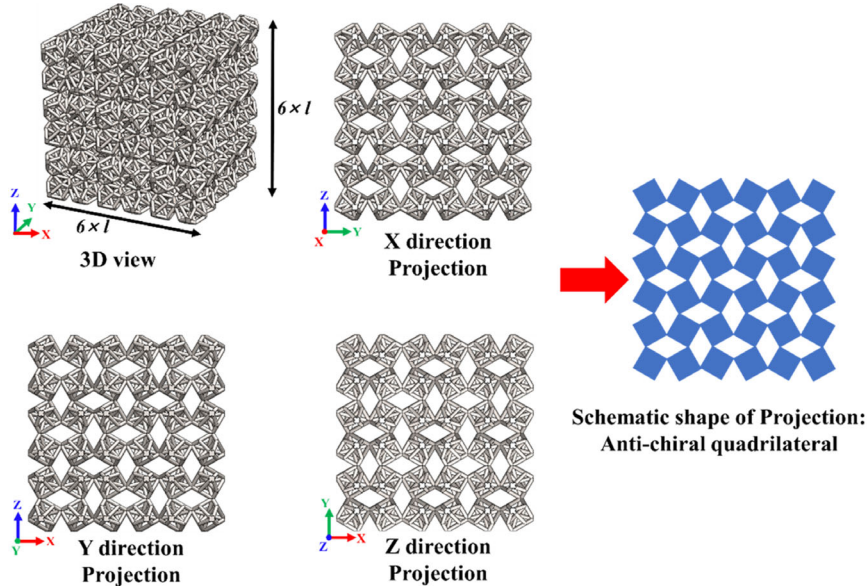


Figure 3. Schematic of the whole A3P-S in this work.

Table 1. List of all nodes and its fractional coordinate in a A3P-UC.

Node type	Node number and its fractional coordinate
PN	P1(0.5, 0.13, 0.13), P2(-0.5, -0.13, -0.13), P3(-0.13, 0.5, 0.13), P4(0.13, -0.5, -0.13), P5(-0.13, -0.13, 0.5), P6(0.13, 0.13, -0.5)
AN	P7(0.27, 0.27, 0.27), P8(-0.27, -0.27, -0.27), P9(0.27, -0.27, -0.27), P10(-0.27, 0.27, 0.27), P11(0.27, 0.27, -0.27), P12(-0.27, -0.27, 0.27), P13(0.27, -0.27, 0.27), P14(-0.27, 0.27, -0.27)

the combination of 27 A3P-IMs arraying along the X, Y, and Z directions, respectively, as shown in Figure 3. To avoid the size effects and reduce the computing time and the preparing cost,

the whole A3P-S in this work contained only three A3P-IMs in three directions (X, Y, and Z).^[7] In addition, this study also built the diamond structure as a comparison,^[36] as shown in Figure 4. To ensure that controlled trials were persuasive, the designed A3P-S and diamond structure samples had the same porosity and number of UC. Both the A3P-S and diamond structures built in this work contained 216 unit cells of their respective types. The specific size parameters of the A3P-S and the diamond structure are listed in Table 2. The design idea of A3P structure was similar to that of 3D-anti-tetra-chiral structure, and the projection shapes were almost the same in X, Y, and Z directions,^[26,28] but the A3P structure did not contain cantilever struts, which was conducive to the formability of LPBF process.

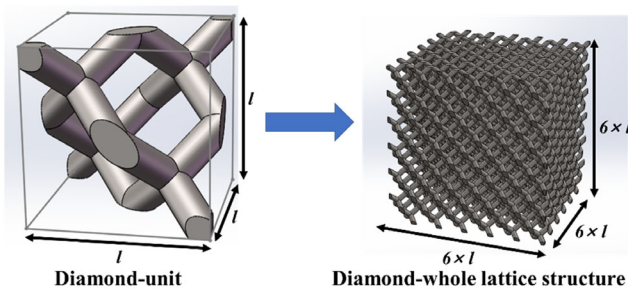


Figure 4. Schematic of the unit cell and whole sample of diamond structure prepared in this work.

2.2. Preparation of Ti-Ta Alloy

Spherical Ta powder (15–45 µm, Suzhou JunDan New Material Science and Technology Co., Ltd.) and spherical Ti powder (15–53 µm, AVI Metal Powder Metallurgy Technology Co., Ltd.) were mixed according to the mass ratio of Ta:Ti = 1:3 (25 wt% Ta, 75 wt% Ti) by a 3D tumble mixer with a speed of 12 r min⁻¹ for 12 h. The morphologies of Ti, Ta, and Ti-Ta mixed powder are shown in Figure 5. The chemical compositions of the powders are displayed in Table 3.

The testing samples were prepared using the EOS M 100 (EOS GmbH, Germany) AM machine. The preparation process was carried out by the serpentine continuous scanning path method and set in an argon atmosphere with oxygen content lower than 0.1% to prevent oxidation of the alloy. The laser power (*P*) and hatching space (*H*) were held at 100 W and 0.06 mm, respectively, and the layer thickness (*L*) was fixed at 0.02 mm during the LPBF process. A scanning strategy was bidirectional scanning where layers were deposited at 67° from each other. The scanning speed (*V*) varied from 100 to 2500 mm s⁻¹. The Ti-Ta tensile bar, A3P-S structure, and diamond structure were built along the *Z* direction with the optimized parameters.

Table 2. Structural parameters of A3P-S and diamond lattice structure.

	Strut diameter <i>d</i> [mm]	unit size <i>l</i> [mm]	Whole size <i>6 × l</i> [mm]	Porosity [%]
A3P-S	0.4	3.5	21	85
Diamond	0.6	3.5	21	85

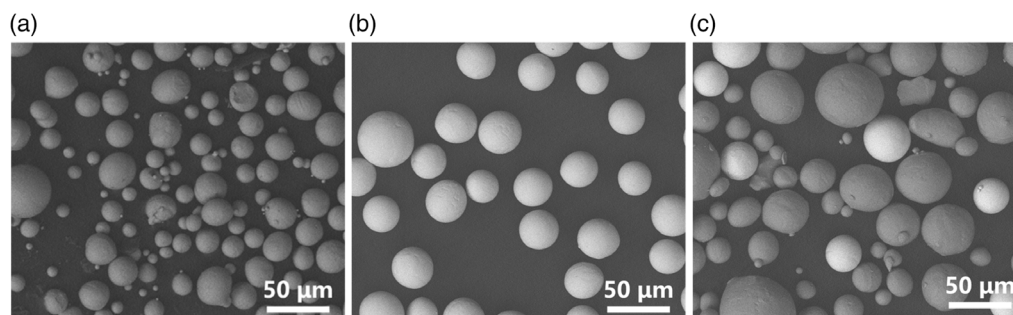


Figure 5. Back-scattered image of mixed Ti, Ta, and Ti-Ta powders showing spherical Ti and Ta particles: a) Ti powder, b) Ta powder, and c) Ti-Ta mixed powder.

(The workpiece exhibits superior mechanical properties perpendicular to the building direction.)^[37] The electrical discharge machining (EDM) process was used to cut the tensile samples from the as-built Ti-Ta bulk sample, according to ASTM B557M-15, as shown in Figure 6.

2.3. FEA

The process of the quasistatic compressive response of the Ti-Ta A3P-S sample was analyzed by FEA simulations with commercial software Abaqus version 6.14 Explicit. The tetrahedral solid elements (3D stress, C3D10M) were used in the FEM model and the average element size was set as 0.2 mm. Two rigid surfaces were built as the upper slider and baseboard of the compressive machine. The uniaxial displacement along the *Y* direction with the rate of 0.001 s⁻¹ was applied on the reference point of the top rigid surface as the load condition. This load rate in FEA was set as same as the compressive experiment. The fully fixed constraint was applied at the reference point of the bottom rigid surface, as shown in Figure 7. The basic material parameters and the hardening curve in the plastic stage of Ti-Ta used in this numerical simulation were obtained from the tensile test in this work (refer to Section 2.4). The loading direction was along the *Y* axis and perpendicular to the build direction (*Z* axis). In addition, to obtain the quasistatic collapse stress during the deformation process, the possibility of damage and interaction of the A3P-S model were considered. The “ductile fracture” criterion was adopted to describe the damage behavior of Ti-Ta material.^[38] The new surfaces were generated in the A3P-S model during the evolution of the damage. Thus, general contact was applied on the contacted surface pairs of the A3P-S model for every face of all elements. The tangential behavior with a friction coefficient of 0.1 and normal behavior with hard contact were defined in contact property for all faces in the sandwich assembly.

2.4. Characterization of Surface Quality and Mechanical Properties

The surface roughness of the as-built Ti-Ta bulk samples with different LPBF parameters was evaluated by a 3D measuring laser microscope (LEXT OLS 4100). The surface perpendicular to the building direction was tested, and the size of the tested area was 2.5 × 2.5 mm². Three duplicated tests at multiple areas

Table 3. Chemical composition of as-received powders, as measured by suppliers.

Ti	Ta	O	Fe	N
Ti	Bal.	—	0.065	0.059
Ta	—	Bal.	0.043	0.047
				0.012

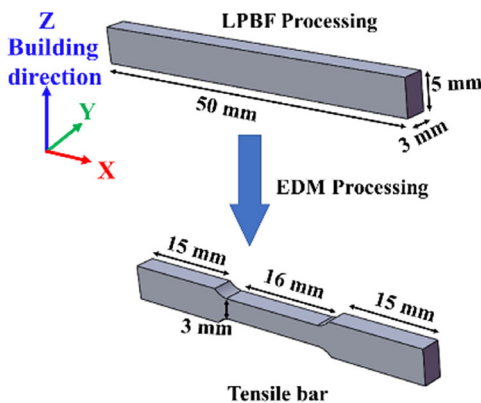


Figure 6. The schematic model for tensile sample fabricated using LPBF.

on each surface were conducted for the surface roughness, and the average value was taken as the result.

The surface, whose normal direction was parallel to the building direction (Z axis) of the bulk sample, was processed for the metallographic analysis and microhardness test. These surfaces of the Ti-Ta samples were ground with SiC sandpaper. Subsequently, the samples were polished by silica suspension (OPS) containing 30% hydrogen peroxide (H_2O_2) for 20 min. Ultrasonic cleaning was conducted using alcohol after polishing.

The quasistatic tensile and compressive properties were conducted by a universal testing machine (CMT-4204). Both tensile and compression tests employed a strain rate of 0.001 s^{-1} . The tensile and compressive curves of each test were determined by taking the average of three samples, respectively. The hardness of the Ti-Ta alloys was evaluated by indentation test using a Vickers hardness tester (HXD-1000TMC/LCD) with a load of 1 kg for 10 s. The microhardness of each sample was determined by

the average of ten indentation tests. A surface parallel to the building direction of samples was selected to conduct the test.

The deformation processes of the A3P samples were recorded by a camera. In order to mitigate the effect of boundary, the square center area containing four A3P-IM structures, which was marked by the yellow dashed frame in **Figure 8**, was selected to calculate the Poisson's ratio. The displacement in the middle area of A3P samples was measured by Image J software, by which the Poisson's ratio ν_{XY} or ν_{ZY} was calculated using the following equation

$$\nu = -\frac{\varepsilon_{X(Z)}}{\varepsilon_Y} \quad (1)$$

where $\varepsilon_{X(Z)}$ and ε_Y were the lateral and vertical strains, respectively. The $\varepsilon_{X(Z)}$ and ε_Y were described using the following equations

$$\varepsilon_Y = \frac{L_a - U_Y}{L_a} \quad (2)$$

$$\varepsilon_{X(Z)} = \frac{L_a - U_{X(Z)}}{L_a} \quad (3)$$

where L_a was the original length of the square middle area; U_Y and $U_{X(Z)}$ were the deformation of lateral and vertical displacement, respectively.

3. Results and Discussion

3.1. LPBF Parameter Optimization for Ti-Ta Alloy

The A3P lattice structure contained many delicate struts and nodes, which required the surface of the LPBF-built metal as flat as possible without seriously deforming during the LPBF process. Otherwise, it would have a negative effect on the precision and mechanical properties of the A3P structure. Moreover, the fine features of A3P structures were very sensitive to defects and deformation. The rough surfaces and irregular laser-scanning weld beads between the interlayers would cause the failure of the A3P-S preparation. In addition, the postprocessing treatment for improving the surface quality was difficult to conduct on the A3P structure. On the other hand, the defects in the LPBF-built bulk materials deteriorated the mechanical properties of the A3P

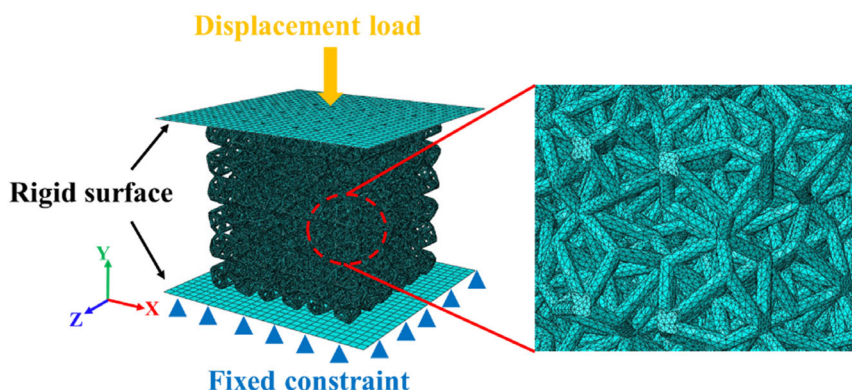


Figure 7. The schematic model of FEA.

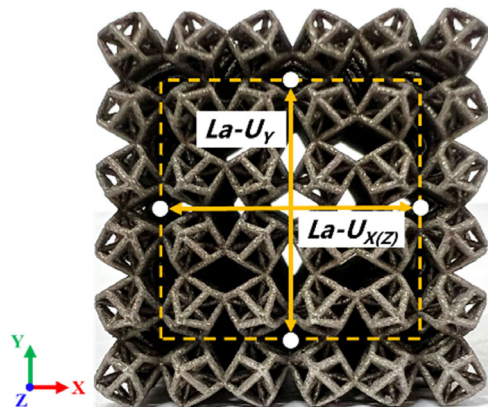


Figure 8. The side view of the A3P-S with yellow dash frame for data collection of La , U_y , $U_{x(z)}$.

structure, so the relative density was also a crucial factor for the parameter optimization of the LPBF process. Therefore, both the surface roughness and the relative density were considered for the parameter optimization of Ti-Ta alloy in this work.

The surface morphologies of samples prepared at six different laser scanning speeds (100 , 200 , 500 , 1000 , 1500 , and 2500 mm s^{-1}) were selected for analysis. The macroscopic photos and local height maps of Ti-Ta alloy samples are shown in **Figure 9**. An identical height scales bar (color bar) was used in all the images

for comparison, as shown in **Figure 9**. The average height of the test surface was defined as the reference height, which was $0\text{ }\mu\text{m}$. When the laser scanning speed was lower than 1000 mm s^{-1} , the laser-scanning weld bead obviously existed on the surface after the LPBF formation, indicating the high surface roughness as shown in **Figure 9a,b,c**. When the laser scanning speed was over 1000 mm s^{-1} , the surface roughness was reduced obviously, as shown in **Figure 9d,e,f**. As shown in **Figure 10**, the surface roughness of the sample decreased with the increase in the laser-scanning speed. When the laser-scanning speed reached 1000 mm s^{-1} , the surface roughness of the sample was the lowest value among these samples. As the laser-scanning speed was above 1000 mm s^{-1} , the surface roughness increased slightly with the increase in the scanning speed.

To further optimize the LPBF parameters for the fabrication of Ti-Ta A3P structures, the relative density of the sample was also analyzed based on the above roughness-related results. The cross-sectional microstructure images of the Ti-Ta bulk samples prepared with the different laser-scanning speeds were compared, as shown in **Figure 11**. When the laser-scanning speed was 100 mm s^{-1} , the laser energy density was the highest, resulting in severe powder spatter and material evaporation during the LPBF process. Many pores were formed in the Ti-Ta sample and the relative density was reduced. As the laser-scanning speed gradually increased, the laser energy density gradually decreased, and the impact of the laser on the molten pool was reduced. The LPBF process became stable and fewer defects generate.

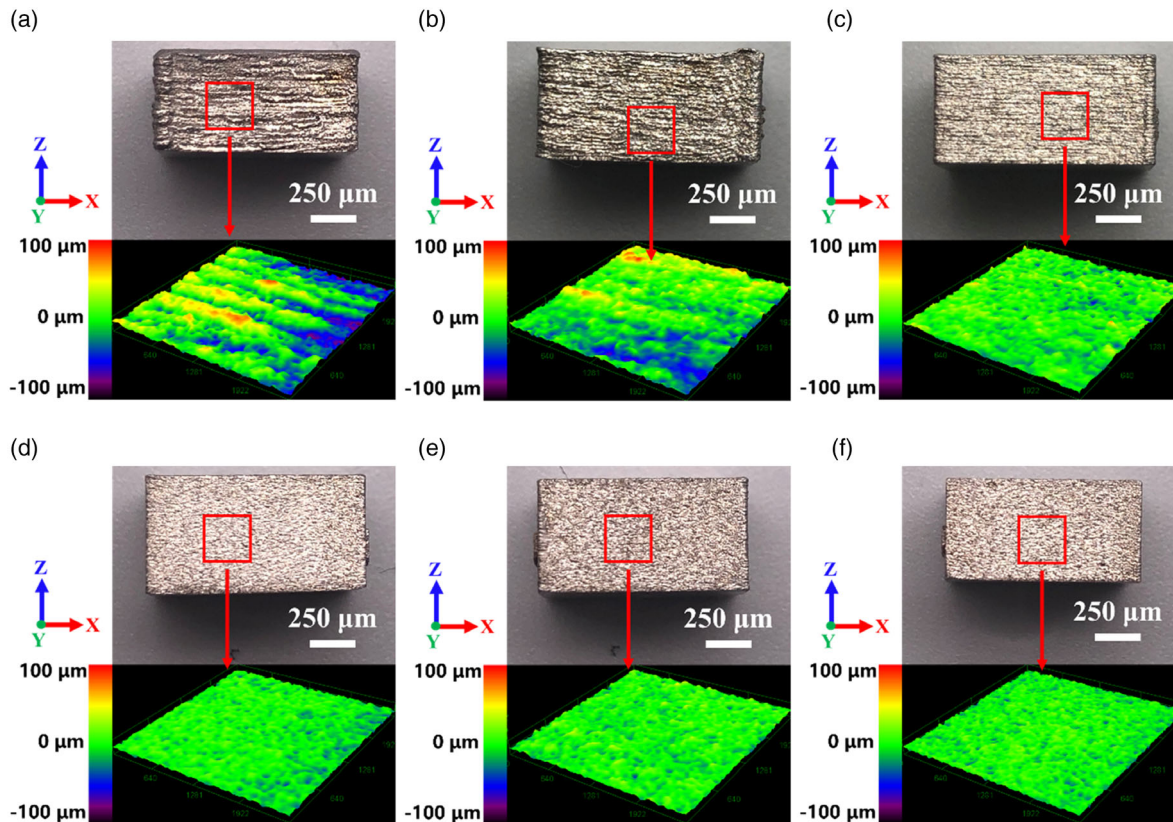


Figure 9. The surface details and height maps of LPBF-built Ti-Ta bulk samples with different laser-scanning speeds (V): a) $V=100$, b) $V=200$, c) $V=500$, d) $V=1000$, e) $V=1500$, and f) $V=2500\text{ mm s}^{-1}$.

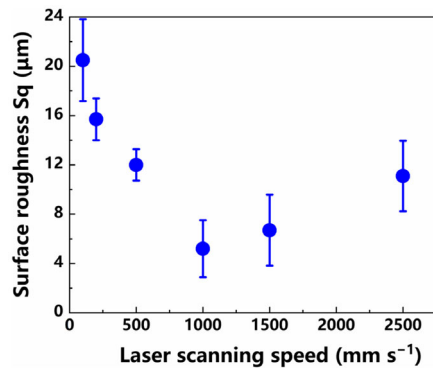


Figure 10. Surface roughness of LPBF-built Ti-Ta alloy with various building parameters.

When the laser-scanning speed was 1000 mm s^{-1} , there were almost no pores distributed in the sample, indicating the high relative density of this sample. As the laser-scanning speed continued to increase, the input energy of the laser was insufficient to melt the metal powder completely, resulting in a large number of defects occurred in the Ti-Ta alloy. In addition, the content of unmelted Ta particles distributed in the Ti-Ta matrix was increased, due to the large difference between the melting points of Ti and Ta.^[35,39] The laser energy was not enough to melt Ta completely under high laser-scanning speed in the LPBF process. As a result of the above analysis, the optimized LPBF parameters for the preparation of the Ti-Ta samples are as follows: $P = 100 \text{ W}$, $H = 0.06 \text{ mm}$, $L = 0.02 \text{ mm}$, and $V = 1000 \text{ mm s}^{-1}$. All the A3P-S and diamond lattice structure samples were built using these LPBF parameters in this work.

To study the elements distribution in LPBF-built Ti-Ta alloy, the surface EDS was conducted. The element distributed map of LPBF-built Ti-Ta samples with different laser scanning speeds was shown in **Figure 12**. As the laser scanning speed increased from 100 to 2500 mm s^{-1} , the average content of Ta element in Ti-Ta alloy was 33.1, 28.6, 28.5, 26.6, 24.7, and 18.0 wt%, respectively. When the laser scanning speed was 100 mm s^{-1} , the laser energy density was the highest among all the Ti-Ta samples, which was 833 J mm^{-3} . The highest laser energy density led to serious Ti evaporation during the LPBF, resulting in higher Ta content than the design value. With the laser scanning speed continuously increasing, the laser energy density gradually decreased, and the evaporation of Ti during the LPBF process reduced, resulting in Ta content gradually close to the designed value (25 wt%). When the laser scanning speed was 1000 mm s^{-1} , the content of the Ta element in Ti-Ta alloy was 26.6 wt%, which was closest to the design value. When the laser scanning speed increased continuously, the laser energy density was significantly reduced, too low a laser energy density led the insufficient melting and poor binding of material. Some unmelted powder was swept off by the scraper and the Ta particles with better fluidity were more easily out of the powder bed, resulting in changes in the content of the Ta elements in the matrix. When the laser scanning speed was 2500 mm s^{-1} , there were plenty of defects in Ti-Ta alloy, and Ti and Ta elements were not sufficiently fused. In this case, a lot of Ta particles were swept away from the powder bed, and the average content of Ta in the Ti-Ta alloy was only 18.0 wt%.

In addition, the more unmelted Ta particles appeared in the Ti-Ta matrix with the higher of laser scanning speed. When the laser scanning speed was $100\text{--}200 \text{ mm s}^{-1}$, the Ta element was uniformly dispersed in the Ti-Ta matrix. When the scanning

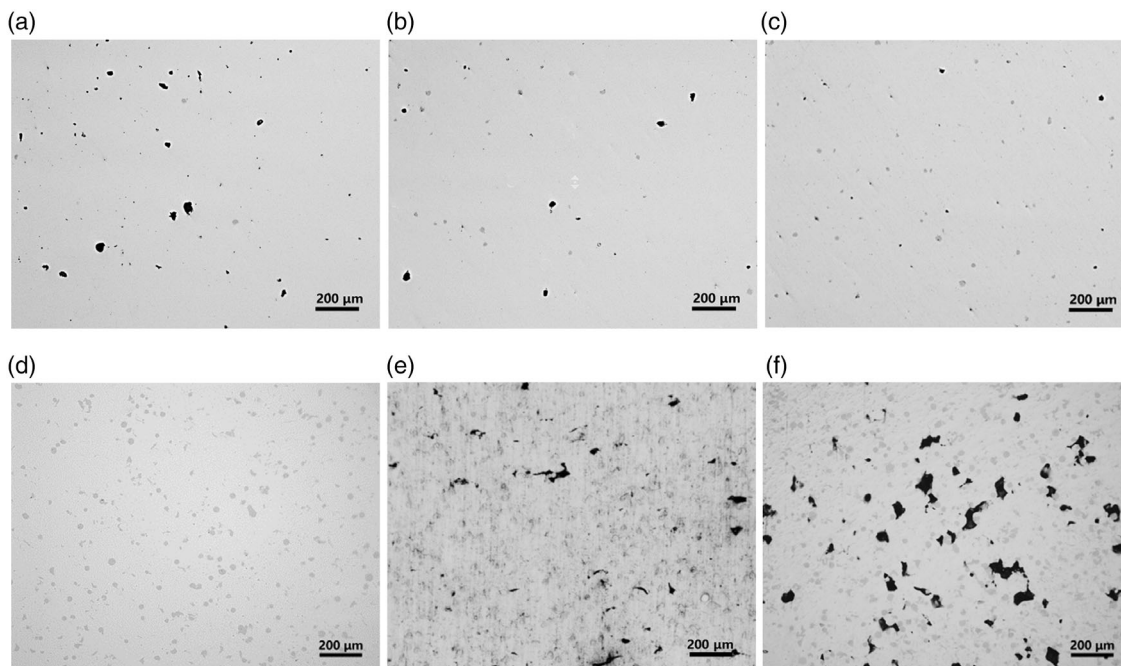


Figure 11. Optical micrograph of XY-sections of LPBF-built Ti-Ta samples prepared with different laser-scanning speeds (V): a) $V = 100$, b) $V = 200$, c) $V = 500$, d) $V = 1000$, e) $V = 1500$, and f) $V = 2500 \text{ mm s}^{-1}$.

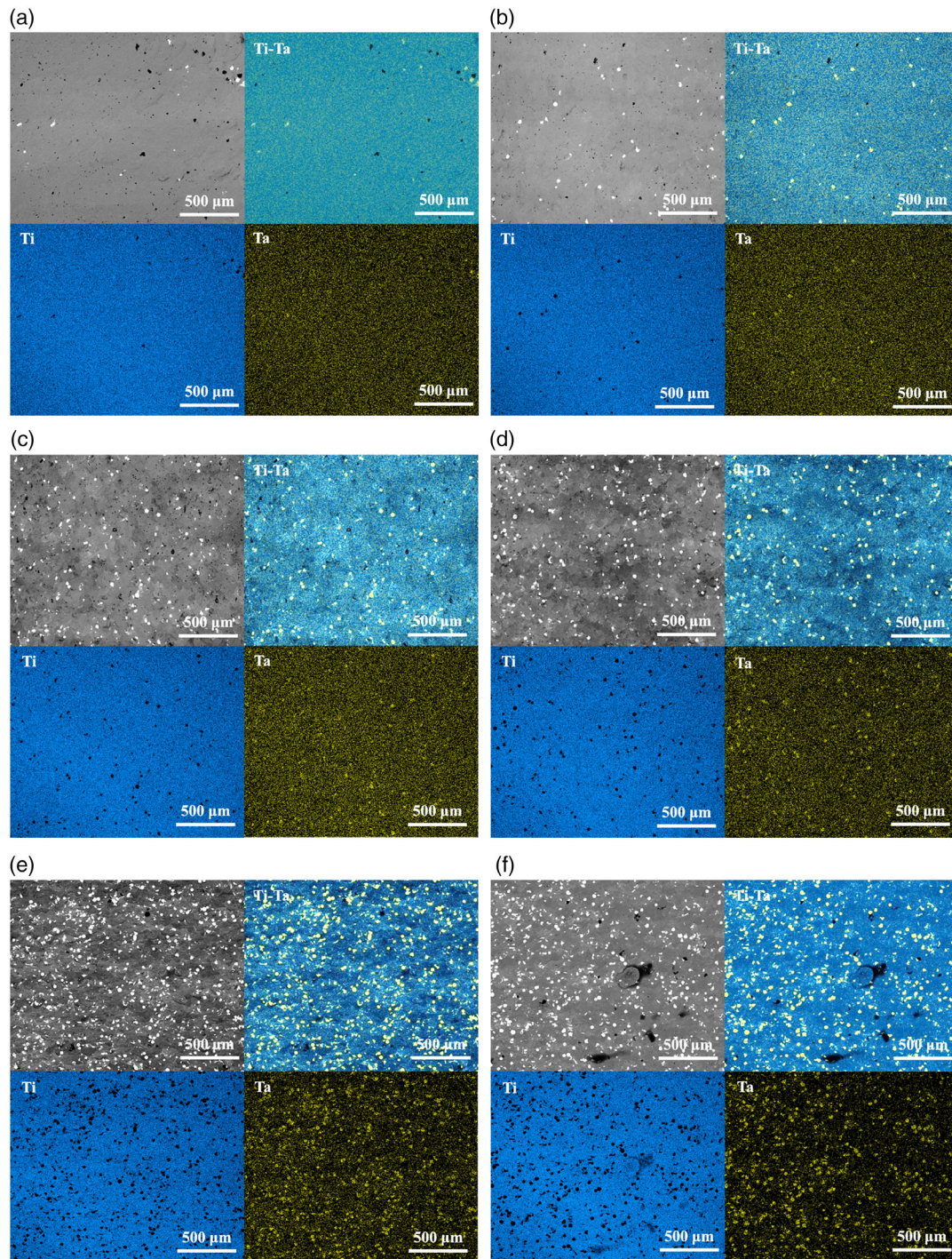


Figure 12. Back-scattered images and EDS surface scan results of XY-sections of LPBF-built Ti-Ta samples prepared with different laser-scanning speeds (V): a) $V = 100$, b) $V = 200$, c) $V = 500$, d) $V = 1000$, (e) $V = 1500$, and f) $V = 2500 \text{ mm s}^{-1}$.

speed was raised to 500–1000 mm s^{-1} , the Ta element did not exist around the unmelted Ta particles, but also in the matrix. However, as the laser scanning speed continued to increase, the Ta element almost only existed around the unmelted Ta particles. The Ta element was not well diffused into the Ti matrix due to the lower laser energy input.

3.2. Mechanical Properties of Ti-Ta Bulk Sample

In this section, the mechanical properties of Ti-Ta bulk samples prepared with the optimized parameters were evaluated. The Ti-6Al-4V and pure Ta bulk samples were also produced by the same machines as the comparison. The properties data

of commercially pure Ti (cp Ti) was referred from Sing's previous study.^[40] The microhardness and stress-strain curves of the above bulk samples were plotted in **Figure 13**. The hardness of Ti-Ta alloy was close to that of Ta and cp Ti, and slightly lower than Ti-6Al-4V, as shown in Figure 13a. The Ti-Ta matrix contained incompletely melted Ta particles as shown in Figure 11 and 12. These Ta particles with low hardness reduced the hardness of the Ti-Ta alloy. The tensile properties of Ti-Ta, Ti-6Al-4V, Ta, and cp Ti were calculated from the stress-strain curve in Figure 13b, as listed in **Table 4**. The elongation of Ti-Ta alloy was more than 3 times that of Ti-6Al-4V which indicated that the LPBF-built Ti-Ta alloy had excellent ductility.

The Ti-Ta samples with the 25 wt% content of Ta mainly consisted of the α' phase, and the pure Ta sample was in the form of the β phase.^[35,41] The existence of unmelted Ta particles in LPBFed Ti-Ta alloy provided the β phase in the Ti-Ta matrix. The structure of the β phase was BCC which effectively improved the toughness and reduced the modulus of the Ti-Ta alloy.^[42,43] The unmelted Ta particles had a special strengthening effect on the mechanical properties of the alloy.^[41,44] The unmelted Ta particles in the Ti-Ta matrix worked as an obstacle for crack propagation, which gave the LPBF-built Ti-Ta good ductility.^[41,45,46] Young's modulus of Ti-Ta alloy was the lowest among all the LPBF-built samples. The yield strength of the Ti-Ta alloy was larger than the LPBF-built Ta and lower than the cp Ti. Thus, the strength-to-modulus ratio (Str M^{-1}) of the LPBFed Ti-Ta alloy was the highest among all samples in this work. As studied by previous researchers, the greater value of Str M^{-1} , the more suitable the material was for the applications of orthopedic implants.^[47-49] Thus, the Ti-Ta alloy

produced by the LPBF process can be a favorable candidate for preparing lattice structures in orthopedic applications.

3.3. Mechanical Properties of the LPBF-Built A3P-S Structure

The quasistatic compression experiments of the A3P-S and diamond samples were conducted perpendicular to the building direction (Y axis) in a universal testing machine. The displacement was precisely controlled during the loading process. The compression tests of each A3P-S and diamond structure were stopped when the maximum displacement reached 10 mm corresponding to the maximum compressive strain ε_Y reached 0.5. Both in A3P-S and diamond structure, the force-displacement curves of FEA and experiment results had the same trend, as shown in **Figure 14**. The loaded result of FEA was higher than that of the experimental result in terms of the same strain value. Because the ideal model of uniform material was used in the FEA model, however, some defects existed in the as-built A3P-S and diamond structure samples, which led to worse mechanical properties.

As plotted in **Figure 14c**, the fracture energy G was calculated from force-displacement curves of A3P-S and diamond structures by the following equation,

$$G = \frac{1}{s} \times \int F d\varepsilon \quad (4)$$

where S was the compressive area of the sample (The compressive surface of the structure was specified as $21 \times 21 \text{ mm}^2$, and the side length of the compressive surface was the same as the whole size $6 \times l$ of the structure.), F was the compressive force,

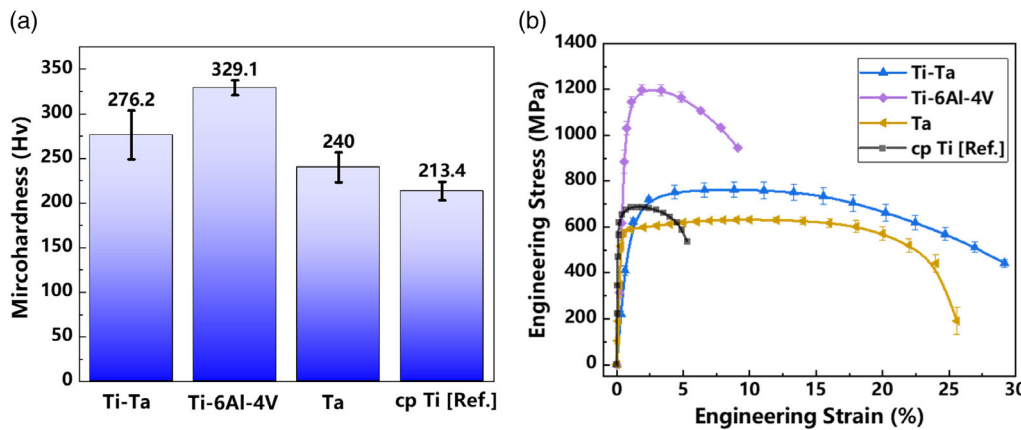


Figure 13. The mechanical properties of LPBF-built Ti-Ta, Ti-6Al-4V, Ta, and cp Ti:^[40] a) the microhardness; b) the stress-strain curve.

Table 4. Tensile properties of LPBF-built Ti-Ta, Ti-6Al-4V, Ta, and cp Ti bulk samples.

Sample name	Yield strength [MPa]	Ultimate tensile strength [MPa]	Elongation [%]	Young's modulus [GPa]	$\text{Str M}^{-1} [10^{-3}]$
Ti-Ta	589 ± 17	771 ± 30	31.0 ± 1.0	65 ± 2	9.06
Ti-6Al-4V	1106 ± 10	1204 ± 15	9.1 ± 0.3	148 ± 1	7.47
Ta	575 ± 16	632 ± 11	26.0 ± 2.6	187 ± 4	3.07
cp Ti ^[40]	620 ± 20	703 ± 16	5.2 ± 0.3	112 ± 3	5.54

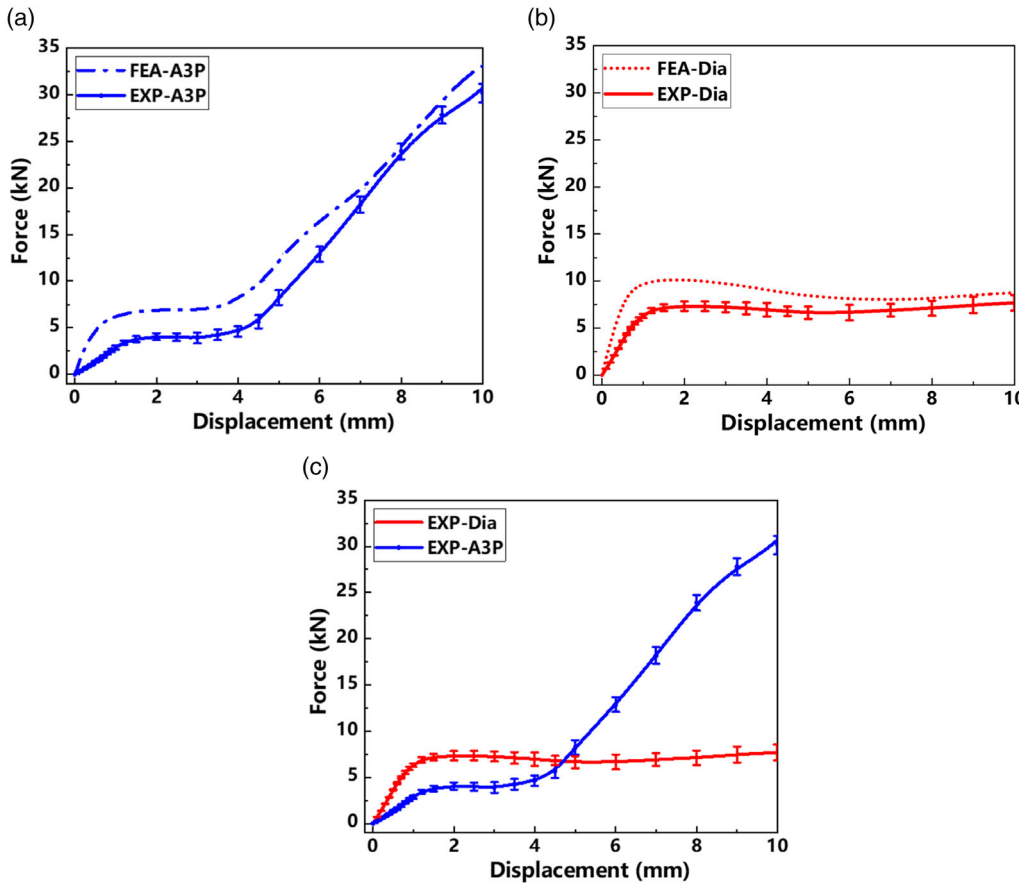


Figure 14. Results of quasistatic collapse of A3P-S and diamond structure compressed in the Y direction: a) experimental and numerical force–displacement curves of A3P-S, b) experimental and numerical force–displacement curves of diamond structure, and c) experimental force–displacement curves of A3P-S and diamond structure.

and ϵ was the strain. The fracture energy of A3P-S and diamond structure was 13.13 and 7.24 J mm^{-3} , respectively. The other mechanical properties in the compression experiment were calculated from the force–displacement curves, as listed in Table 5. The A3P-S had higher fracture energy than that of the diamond structure. If the two structures are applied to the human body as orthopedic implants, when the human body suffers severe impact or load force, the A3P structure can absorb more energy from the impact than the typical diamond structure. The experimental results reflected the advantages of the A3P structure in the orthopedic application. In comparison with the diamond structure, the A3P structure had a lower modulus and was more compatible with the human body.

Table 5. Tensile properties of LPBF-built Ti-Ta, A3P-S and diamond structure.

Sample name	Yield strength [MPa]	Compressive strength [MPa]	Young's modulus [GPa]
A3P-S	9.2 ± 0.42	54.3 ± 2	0.14 ± 2
Diamond	15.6 ± 0.38	19.9 ± 0.2	0.34 ± 1

To study the quasistatic collapse behavior, the experimental deformation results of the A3P-S and diamond structure samples at strains of 0.125 , 0.25 , 0.375 , and 0.5 in the compressive experiment were compared with the FEA results, as shown in Figure 15, indicating the FEA result had a good agreement with the experimental results. The deformation process of the A3P-S showed a strong auxetic behavior during the quasistatic compressive process. Every unit of the A3P-S structure rotated during the compression process. The rotation and shrinkage of each A3P-UC resulted in the continuous transverse contraction of the whole A3P-S. When ϵ_Y reached 0.2 , the struts in each A3P-UC began to contact with each other, and the load–displacement curve of A3P-S increased distinctly. In addition, the stress distribution map of FEA indicated that the stress first concentrated at the primary node in the A3P-UC during the compressive process. As the A3P-S gradually collapsed, the stress was begun to appear at internal struts. The deformation process of the diamond structure showed a positive Poisson's ratio and the sample expands appreciably perpendicular to the compressive direction during the quasistatic compressive process. Both FEA and experimental test results showed that when the diamond structure was collapsing, the failure occurs along the 45° of the compressive direction.

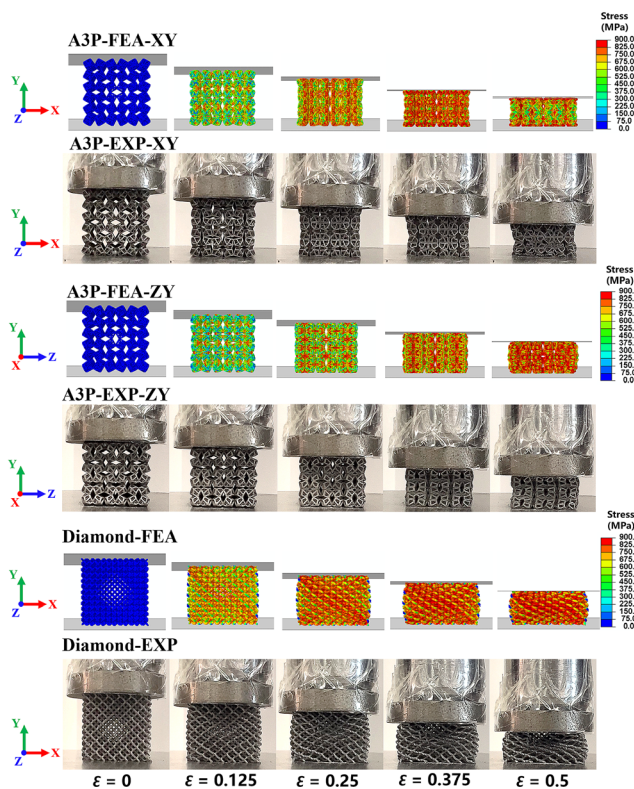


Figure 15. Deformation status of A3P-S and diamond structure at $\epsilon_Y = 0, 0.125, 0.25, 0.375$, and 0.5 .

The elastic stage of the A3P-S was extended longer than that of the diamond structure. In the actual biological application, the structures failed when the plastic deformation started. In this way, the A3P structure can withstand large strains without failure. When the deformation of A3P-S was about 4 mm ($\epsilon_Y = 0.2$), the load force of the A3P-S increased significantly, indicating the internal components of the A3P-S started to contact each other. However, the force–displacement curves of the diamond structure did not show a sharp rise, indicating the internal components of the diamond structure were not completely contacted, as shown in Figure 15. With the increase of deformation, the A3P-S had an obvious transverse contraction, while the diamond structure expanded, indicating a negative Poisson's ratio effect in the A3P structure. At last, the A3P-S started to collapse from the bottom layer while the diamond structure's failure started from the center.

The deformation contour results of the A3P-S and diamond structure during the compressive simulation are shown in Figure 16 and 17, respectively. The red color indicated the increase of displacement along the positive direction of the $X(Z)$ axis, while the blue color indicated the increase of displacement along the negative direction of X and Z axes. As shown in Figure 16, the transverse contractions (along X and Z axes) were generated when the A3P-S were compressed vertically along the Y axis. In addition, from the displacement map in Figure 16, it was found that both sides of the A3P-S in the X and Z direction moved synchronously toward the center of the structure. However, the diamond structure exhibited the inverse performance during the compressive process (Figure 17). The diamond

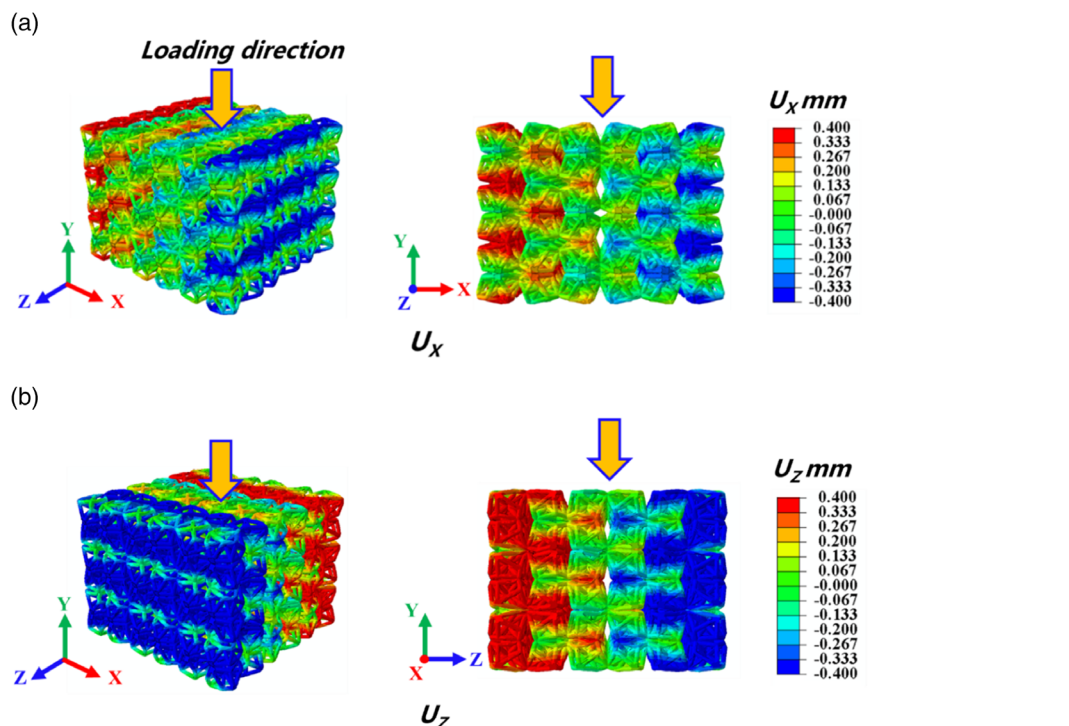


Figure 16. The transverse displacement of A3P-S in different directions at ϵ_Y of 0.25 : a) the displacement along the X axis (U_X), and b) the displacement along the Z axis (U_Z).

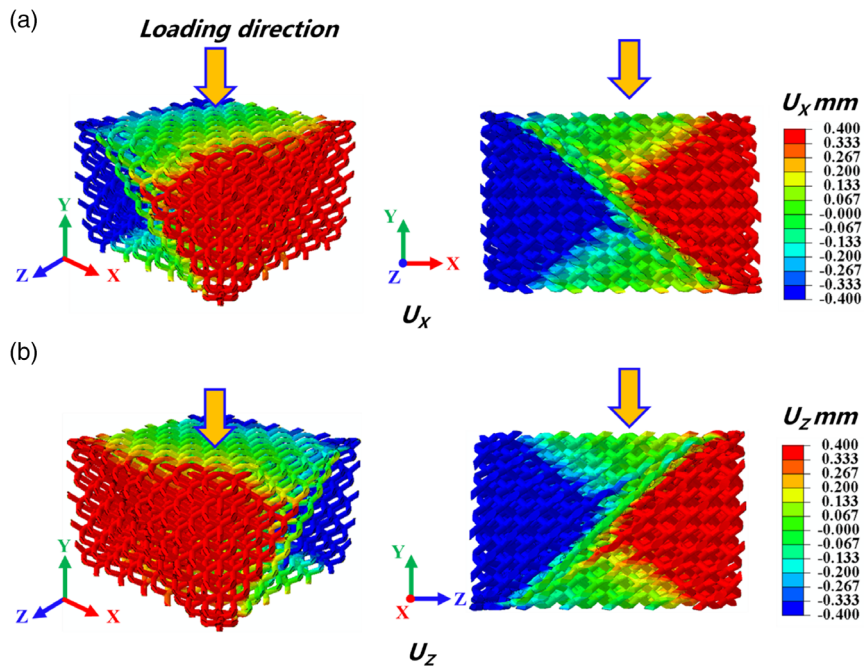


Figure 17. The transverse displacement of diamond structure in different directions at ϵ_Y of 0.25: a) the displacement along the X axis (U_x), and b) the displacement along the Z axis (U_z).

structure expanded along the X and Z directions, and the projection view of the X and Z directions showed a failure trend along the 45° of the compressive direction. The projective morphologies in the Y direction of the A3P-S and diamond structure after the compressive test were shown in **Figure 18**. Perpendicular to the compressive direction, the dimension of the A3P-S decreased, but the dimension of the diamond structure increased obviously. In both A3P-S and diamond structures, severe plastic deformation occurred during compression according to the results of the FEA and compressive test. The A3P auxetic structure and diamond structure did not return to their original shape after compression.

The Poisson's ratio of A3P structure as a function of strain ϵ_Y is plotted in **Figure 19**. Both FEA and experimental results showed that the Poisson's ratio of A3P-S in XY plane and ZY plane was in a similar "S-curve" trend with only a little difference in value, indicating the reliability of the FEA simulations in this work. The Poisson's ratio of v_{XY} was a little lower than v_{ZY} in the A3P-S structure which indicated the deformation of shrinkage in the X direction was slightly larger than that in the Z direction. Although the projection of the A3P structure on X, Y, and Z was a 2D antichiral quadrilateral, there was still little difference in the arrangement of struts and the position of contact nodes.

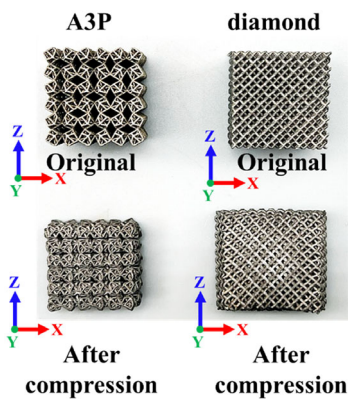


Figure 18. The projective morphologies in Y direction of the A3P-S and diamond structure after compressive test compared with their original structures respectively.

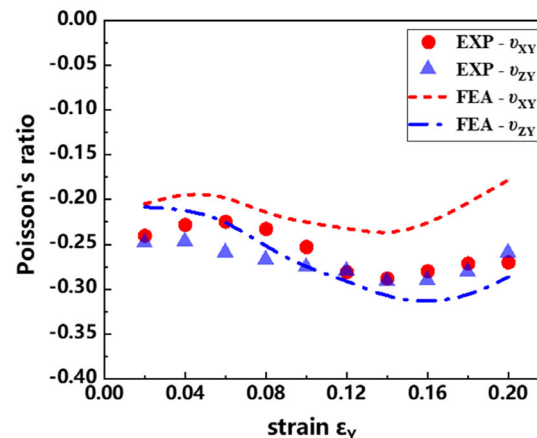


Figure 19. The numerical and experimental results of the Poisson's ratio.

4. Conclusion

In this article, a novel A3P structure was designed and prepared using Ti-Ta materials by LPBF technology. The content of Ti and Ta was 75 and 25 wt% respectively. The surface roughness and relative density of the LPBF-built Ti-Ta samples with different laser-scanning speeds were investigated. The mechanical responses of the A3P under uniaxial compression were investigated by experiments and FEA simulations. In addition, a traditional diamond lattice structure was also prepared as a comparison to the A3P structure. These two structures have exhibited different mechanical behaviors. The specific results can be summarized as follows. 1) The surface roughness and relative density of Ti-Ta bulk samples prepared by different LPBF process parameters were evaluated. With increasing laser scanning speed (i.e., the laser energy density decreased), the surface roughness of Ti-Ta alloy initially decreased and then increased. In addition, when laser-scanning speed was above 1000 mm s^{-1} , the relative density reduced with the increase of the laser-scanning speed. As a result, the LPBF formation quality of the Ti-Ta bulk sample deteriorated by too-low and too-high laser-scanning speeds. In this study, the following LPBF parameters were selected for the preparation of the A3P-S and diamond structures: $P = 100 \text{ W}$, $H = 0.06 \text{ mm}$, $L = 0.02 \text{ mm}$, and $v = 1000 \text{ mm s}^{-1}$. 2) The FEA results showed that the A3P structures had the behavior of negative Poisson's ratio during the compression process which was consistent with the experimental results. In the compression process, the stress first concentrated on the primary node of the A3P-UC, and then the A3P-UC started to rotate obviously. In general, the A3P-S structure showed a negative Poisson's ratio behavior in both X and Z directions during the compression process. 3) According to the results of the compressive experiment, when the compression was up to 10 mm ($\epsilon_y = 0.5$), the A3P-S and diamond structure collapsed obviously. The compressive strength of the A3P-S was 54.3 MPa , which was larger than that of the diamond structure (19.9 MPa). The fracture energy of A3P-S (13.13 J mm^{-3}) was also larger than that of the diamond structure (7.24 J mm^{-3}), suggesting the A3P structure had better resistance to break than the diamond structure. The elastic modulus of A3P-S (0.14 GPa) was lower than that of the diamond structure (0.34 GPa), indicating the A3P structure had better modulus compatibility with human bone. In conclusion, the A3P structure with Ti-Ta prepared by LPBF technology has great potential in the future application of orthopedic implants.

Acknowledgements

The authors would like to thank the financial support to this work from the General Program of Science and Technology Development Project of Beijing Municipal Education Commission (grant no. KM202010005006).

Conflict of Interest

The authors declare no conflict of interest.

Data Availability Statement

The data that support the findings of this study are available from the corresponding author upon reasonable request.

Keywords

auxetic material, laser powder bed fusion, mechanical performance, metamaterials, Ti-Ta alloys

Received: February 21, 2023

Revised: May 4, 2023

Published online: May 18, 2023

- [1] X. Hou, Z. Deng, K. Zhang, *Acta Mech. Solida Sin.* **2016**, 5, 490.
- [2] P. Bettini, A. Airolidi, G. Sala, L. D. Landro, M. Ruzzene, A. Spadoni, *Composites, Part: B* **2010**, 41, 133.
- [3] K. E. Evans, A. Alderson, *Adv. Mater.* **2000**, 12, 617.
- [4] A. A. Zadpoor, *Acta Biomater.* **2019**, 85, 41.
- [5] M. Gao, D. Y. He, X. Y. Guo, H. R. Wu, Z. Tan, X. Wu, W. Shao, G. H. Wang, *Structures* **2022**, 44, 1219.
- [6] I. P. Seetoh, X. Y. Liu, K. Markandan, L. Zhen, C. Q. Lai, *Mech. Mater.* **2021**, 156, 103811.
- [7] Q. S. Wang, Z. Y. Yang, Z. X. Lu, X. Li, *Mater. Des.* **2020**, 186, 108226.
- [8] A. A. Zadpoor, *Biomater. Sci.* **2020**, 8, 18.
- [9] S. Li, H. Hassanin, M. M. Attalla, N. J. E. Adkins, K. Essa, *Acta Mater.* **2016**, 105, 75.
- [10] D. Li, J. H. Yin, L. Dong, R. S. Lakes, *J. Mater. Sci.* **2018**, 53, 3493.
- [11] A. Clausen, F. W. Wang, J. S. Jensen, O. Sigmund, J. A. Lewis, *Adv. Mater.* **2015**, 27, 5523.
- [12] D. Prall, R. S. Lakes, *Int. J. Mech. Sci.* **1997**, 39, 305.
- [13] K. Kuribayashi, K. Tsuchiya, Z. You, D. Tomus, M. Umemoto, T. Ito, M. Sasaki, *Mater. Sci. Eng., A* **2006**, 419, 131.
- [14] H. M. Kolken, S. Janbaz, S. M. Leeflang, K. Lietaert, H. H. Weinans, A. A. Zadpoor, *Mater. Horiz.* **2018**, 5, 28.
- [15] S. B. Goodman, *Biomaterials* **2007**, 28, 5044.
- [16] P. A. Revell, *J. R. Soc., Interface* **2008**, 5, 1263.
- [17] M. Sundfeldt, L. V. Carlsson, C. B. Johansson, P. Thomsen, C. Gretzer, *Acta Orthop.* **2006**, 77, 177.
- [18] J. N. Grima, P. S. Farrugia, R. Gatt, D. Attard, *Phys. Status Solidi B* **2008**, 245, 521.
- [19] L. J. Gibson, M. F. Ashby, G. S. Schajer, C. I. Robertson, *J. Math. Phys. Sci.* **1982**, 382, 25.
- [20] D. Mousanezhad, B. Haghpanah, R. Ghosh, A. M. Hamouda, N. H. Hashemi, A. Vaziri, *Theor. Appl. Mech. Lett.* **2016**, 6, 81.
- [21] D. Bornengo, F. Scarpa, C. Remillat, in *Proc. Inst. Mech. Eng., Part G* **2005**, Vol. 219, p. 185.
- [22] L. Yang, O. Harrysson, H. Westb, D. Cormier, *Int. J. Solids Struct.* **2015**, 69–70, 475.
- [23] H. Yang, B. Wang, L. Ma, *Int. J. Solids Struct.* **2019**, 180–181, 13.
- [24] K. K. Saxena, R. Das, E. P. Calius, *Adv. Eng. Mater.* **2016**, 18, 1847.
- [25] L. Mizzi, E. M. Mahdi, K. Titov, R. Gatt, D. Attard, K. E. Evans, J. P. Grima, J. C. Tan, *Mater. Des.* **2018**, 146, 28.
- [26] H. H. Huang, B. L. Wong, Y. C. Chou, *Phys. Status Solidi B* **2016**, 253, 1557.
- [27] Q. Q. Zhang, J. Q. Dong, Y. T. Zhao, Y. Y. Zheng, *Int. J. Smart Nano Mater.* **2022**, 13, 152.
- [28] X. Fei, L. Jin, X. J. Zhang, X. Li, M. H. Lu, *Appl. Phys. Lett.* **2020**, 116, 021902.
- [29] M. Mohsenizadeh, F. Gasbarri, M. Munther, A. Beheshti, K. Davami, *Mater. Des.* **2018**, 139, 521.
- [30] J. X. Fan, L. Zhang, S. S. Wei, Z. Zhang, S. K. Choi, B. Song, Y. S. Shi, *Mater. Today* **2021**, 50, 303.
- [31] Y. Qin, P. Wen, H. Guo, D. Xia, Y. Zheng, L. Jauer, R. Poprawe, M. Voshage, J. H. Schleifenbaum, *Acta Biomater.* **2019**, 98, 3.
- [32] S. Huang, S. L. Sing, G. D. Looze, R. Wilson, W. Y. Yeong, *J. Mech. Behav. Biomed. Mater.* **2020**, 108, 103775.

- [33] Y. L. Zhou, M. Niinomi, T. Akahori, *Mater. Sci. Eng., A* **2004**, *371*, 283.
- [34] Y. L. Zhou, M. Niinomi, *Mater. Sci. Eng., C* **2009**, *29*, 1061.
- [35] E. G. Brodie, A. E. Medvedev, J. E. Frith, M. S. Dargusch, H. L. Fraser, A. Molotnikov, *J. Alloys Compd.* **2020**, *820*, 153082.
- [36] H. Wang, K. X. Su, L. Z. Su, P. P. Liang, P. Ji, C. Wang, *Mater. Sci. Eng., C* **2019**, *104*, 109908.
- [37] T. Maconachie, M. Leary, J. J. Zhang, A. Medvedev, A. Sarker, D. Ruan, G. X. Lu, O. Faruque, M. Brandt, *Mater. Sci. Eng., A* **2020**, *788*, 139445.
- [38] H. Hooputra, H. Gese, H. Dell, H. Werner, *Int. J. Crashworthiness* **2004**, *9*, 449.
- [39] L. L. Xing, C. C. Zhao, H. Chen, Z. J. Shen, W. Liu, *Acta Metall. Sin.* **2020**, *33*, 981.
- [40] S. L. Sing, W. Y. Yeong, F. E. Wiria, *J. Alloys Compd.* **2016**, *660*, 461.
- [41] E. G. Brodie, J. Richter, T. Wegener, T. Niendorf, A. Molotnikov, *Mater. Sci. Eng., A* **2020**, *798*, 140228.
- [42] M. Niinomi, *J. Artif. Organs* **2008**, *35*, 359.
- [43] D. Raducanu, V. D. Cojocaru, A. Nocivin, I. Cinca, N. Serban, E. M. Cojocaru, *JOM* **2020**, *72*, 2937.
- [44] D. L. Zhao, C. J. Han, Y. Li, J. J. Li, K. Zhou, Q. S. Wei, J. Liu, Y. S. Shi, *J. Alloys Compd.* **2019**, *804*, 288.
- [45] S. Huang, R. L. Narayan, J. H. K. Tan, S. L. Sing, W. Y. Yeong, *Acta Mater.* **2021**, *204*, 116522.
- [46] S. Huang, P. Kumar, W. Y. Yeong, R. L. Narayan, U. Ramamurty, *Acta Mater.* **2022**, *225*, 117593.
- [47] Y. Song, D. S. Xu, R. Yang, D. Li, W. T. Wu, Z. X. Guo, *Mater. Sci. Eng., A* **1999**, *A260*, 269.
- [48] Y. L. Zhou, M. Niinomi, T. Akahori, *Mater. Trans.* **2004**, *45*, 1549.
- [49] X. L. Zhao, M. Niinomi, M. Nakai, T. Ishimoto, T. Nakano, *Mater. Sci. Eng., C* **2011**, *31*, 1436.